

## Reshaping hydrogen bond network in aqueous-aprotic hybrid electrolyte to achieve highly selective ambient ammonia synthesis

Jiajie Ni <sup>a,b,1</sup>, Qiyang Cheng <sup>b,1</sup>, Mengfan Wang <sup>b,\*</sup>, Sisi Liu <sup>c</sup>, Haoqing Ji <sup>b</sup>, Yanzheng He <sup>b</sup>, Tao Qian <sup>c</sup>, Chenglin Yan <sup>b,d,\*\*</sup>, Jianmei Lu <sup>a,\*</sup>

<sup>a</sup> College of Chemistry, Chemical Engineering and Materials Science, Soochow University, Suzhou 215006, China

<sup>b</sup> Key Laboratory of Core Technology of High Specific Energy Battery and Key Materials for Petroleum and Chemical Industry, College of Energy, Soochow University, Suzhou 215006, China

<sup>c</sup> School of Chemistry and Chemical Engineering, Nantong University, Nantong 226019, China

<sup>d</sup> School of Petrochemical Engineering, Changzhou University, Changzhou 213164, China



### ARTICLE INFO

#### Keywords:

Aqueous-aprotic hybrid electrolyte  
Hydrogen bond network  
Trimethyl phosphate  
Ammonia synthesis  
Nitrogen reduction reaction

### ABSTRACT

Aqueous electrolytes are extensively applied in electrochemical nitrogen reduction reaction, while the overwhelming  $\text{H}_2\text{O}$  always produce much protons, favoring the electron-stealing hydrogen evolution reaction (HER) and thus leaving the current ammonia synthesis much to be desired. Here, we propose an aqueous-aprotic hybrid electrolyte system by introducing trimethyl phosphate (TMP) as a cosolvent to achieve highly selective ammonia synthesis. TMP features higher Gutmann donors than that of  $\text{H}_2\text{O}$ , preferring to serve as hydrogen bond (HB) acceptor and reshaping the HB network in the electrolyte. Molecular dynamics simulations suggest that, compared with  $\text{H}_2\text{O}-\text{H}_2\text{O}$  HB, the  $\text{H}_2\text{O}-\text{TMP}$  HB exhibits longer lifetime and better stability. The intensified interaction between  $\text{H}_2\text{O}$  and TMP weakens the interaction between  $\text{H}_2\text{O}$  and  $\text{H}_2\text{O}$ , which strengthens the O-H bond of  $\text{H}_2\text{O}$  and makes it more difficult to be broken, thus greatly inhibiting the dissociation of  $\text{H}_2\text{O}$  and leading to a suppressed HER activity. Correspondingly, a significantly improved NRR performance with a superior  $\text{NH}_3$  yield rate of  $82.1 \pm 2.7 \mu\text{g h}^{-1} \text{ mg}^{-1}$  and an optimum Faradaic efficiency of  $73.3 \pm 2.7\%$  is achieved in the  $\text{H}_2\text{O}-\text{TMP}$  hybrid electrolyte, indicative of order of magnitude enhancement compared with that delivered in the conventional aqueous electrolyte.

### 1. Introduction

Ammonia ( $\text{NH}_3$ ), as an essential precursor in fertilizer production as well as a promising energy carrier due to its high hydrogen content [1–4], is currently produced via the long-standing Haber-Bosch process under harsh operating conditions. However, the conversion ratio of this energy-intensive process is extremely low owing to the unfavorable chemical equilibrium and the subsequent  $\text{CO}_2$  release problem also exacerbates environmental pressures [5–8]. In this case, the exploring of alternative routes is of great importance. Theoretical studies and previous research have proven that electrochemical nitrogen reduction reaction (NRR) is feasible for green ammonia synthesis [9–12], which holds great potential to replace the Haber-Bosch process. The proposed

mechanisms of the NRR process are divided into the alternating pathway and distal pathway, based on different hydrogenation sequences. In alternating pathway, the two N atoms are hydrogenated successively until the two  $\text{NH}_3$  molecules are released sequentially at the last two steps. By contrast, in the distal pathway, the distal N is continuously hydrogenated until the release of the first  $\text{NH}_3$ , followed by the hydrogenation of the remaining N to yield the second  $\text{NH}_3$ . To date, the vast majority of researches emphasize on developing novel electrocatalysts and a variety of strategies have been put forward to reduce the thermodynamic energy barrier and enhance the NRR performance [13–19]. Unfortunately, the presented  $\text{NH}_3$  yield rate and Faradaic efficiency remain low, which are far from the requirements of industrial production [20,21]. Therefore, it is urgent to look beyond electrocatalyst and

\* Corresponding authors.

\*\* Corresponding author at: Key Laboratory of Core Technology of High Specific Energy Battery and Key Materials for Petroleum and Chemical Industry, College of Energy, Soochow University, Suzhou 215006, China.

E-mail addresses: [mfwang1204@suda.edu.cn](mailto:mfwang1204@suda.edu.cn) (M. Wang), [c.yan@suda.edu.cn](mailto:c.yan@suda.edu.cn) (C. Yan), [lujm@suda.edu.cn](mailto:lujm@suda.edu.cn) (J. Lu).

<sup>1</sup> These authors contributed equally to this work

achieve breakthrough from other point of view.

The NRR process predominantly take place in the multiphase interface region among the liquid electrolyte, solid electrocatalyst, and gaseous nitrogen [22–24]. That is, the electrolyte highly participates in the reaction process and plays a vital role in determining the electrochemical performance [25,26]. Aqueous electrolytes are extensively applied in most cases at present. Unfortunately, the overwhelming  $\text{H}_2\text{O}$  in aqueous electrolyte always produce much protons, favoring the electron-stealing hydrogen evolution reaction (HER) owing to readily availability of protons and the extremely close standard reduction potential of nitrogen compared with HER [27–30]. Considering the trade-off between NRR and HER, the suppression of HER is vitally important for promoting the NRR process [31,32]. The water dissociation step, that is, the Volmer step, has been proposed as a main kinetic limitation of HER, which is greatly affected by the hydrogen bond environment in the electrolyte [33,34]. In this case, it would be highly desirable to introduce a suitable cosolvent that could break the original hydrogen bond (HB) network in the traditional aqueous electrolyte and manipulate the structure of water molecules from long-range organization to isolated state [35,36]. If so, the activity of free water could be decreased to a great extent, thus inhibiting the transport of protons through the Grotthuss diffusion mechanism and effectively suppressing the HER [37,38].

Herein, we chose trimethyl phosphate (TMP), a type of aprotic solvent and HB acceptor agent, to serve as a cosolvent and developed a novel aqueous-aprotic hybrid electrolyte system for ammonia synthesis under ambient conditions (Fig. 1a). TMP features higher electron-donating ability than  $\text{H}_2\text{O}$ , so that the H of O-H in  $\text{H}_2\text{O}$  molecules

prefer to interact with O of P=O bond in TMP molecules rather than adjacent  $\text{H}_2\text{O}$  molecules, forming the HB between TMP and  $\text{H}_2\text{O}$  [39]. Theoretical simulations and experimental results confirm that the addition of TMP effectively reconstructs the HB network in the hybrid electrolyte. The generation of intensified HB between TMP and  $\text{H}_2\text{O}$  enhances the strength of O-H bond in  $\text{H}_2\text{O}$ , making it more difficult to be broken and thus inhibiting the water dissociation. As expected, when this novel electrolyte system was coupled with RhCo dispersed N-C (RhCoNC) derived from metal-organic framework (MOF) as efficient electrocatalyst, the HER process was suppressed to a certain extent and a superior NRR performance with the maximum  $\text{NH}_3$  yield rate of  $82.1 \pm 2.7 \mu\text{g h}^{-1} \text{ mg}^{-1}$  and the optimum Faradaic efficiency of  $73.3 \pm 2.7\%$  was achieved at  $-1.5$  V versus (vs.) Ag/AgCl. This work provides new insight into electrolyte design and sheds light on highly selective ambient ammonia synthesis.

## 2. Experimental section

### 2.1. MD simulation method and model

Molecular dynamics simulations were performed with Gromacs 2019.6.  $40 \text{ Na}^+/\text{ClO}_4^-$  were randomly dispersed in a cubic simulation box with an edge length of  $\sim 5 \text{ nm}$ . Then, five simulation systems were constructed by solvating the box with different number of water and TMP molecules. Parameters of  $\text{Na}^+$  and  $\text{ClO}_4^-$  were obtained from the work of Merz et al. and Acevedo et al., respectively. TMP was modelled by the OPLS-AA Force Field. Water was described by the SPC/E model. Electrostatic interactions were calculated with the particle-mesh Ewald

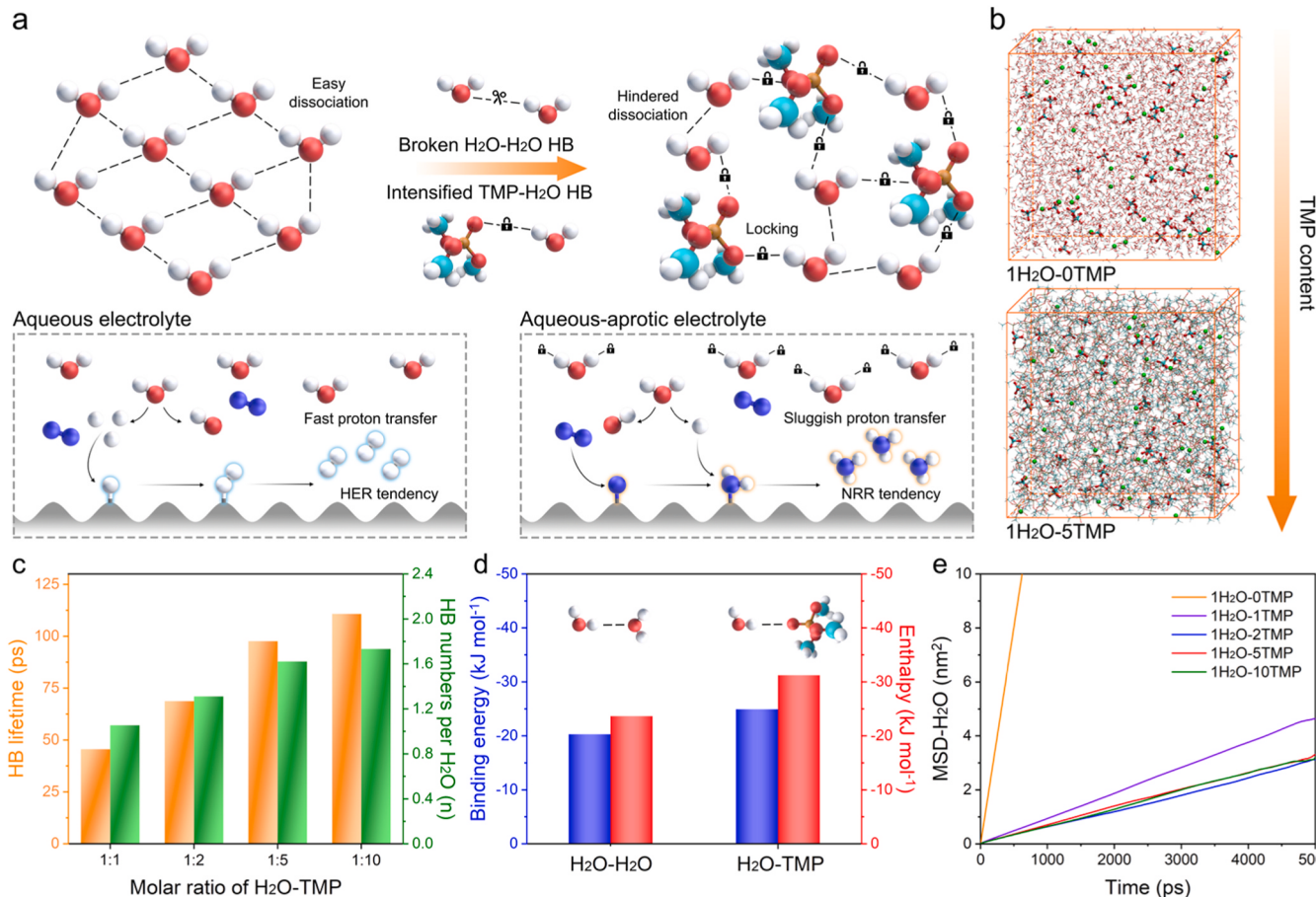


**Fig. 1.** (a) Schematic illustration of the NRR and HER processes in the aqueous and aqueous-aprotic hybrid electrolytes, respectively. (b) Snapshots of the hybrid electrolyte systems with the  $\text{H}_2\text{O}$ -TMP molar ratio of 1:0 and 1:5, respectively. (c) HB lifetime and HB numbers per  $\text{H}_2\text{O}$  in the  $\text{H}_2\text{O}$ -TMP hybrid electrolytes with different molar ratios. (d) Binding energies and enthalpies of  $\text{H}_2\text{O}$ -TMP and  $\text{H}_2\text{O}$ - $\text{H}_2\text{O}$ . (e) The MSD of  $\text{H}_2\text{O}$  in the different electrolytes.

method. Van der Waals interactions were described by Lennard Jones (LJ) potential truncated at 1.2 nm, with the LJ parameters between different atom pairs derived by Lorentz-Berthelot mixing rules. Initial configurations were energy-minimized by steepest-descent algorithm, followed by equilibration at 298.15 K and 1.0 bar for 1 ns. Then 10-ns production runs were carried out under NPT ensemble with v-rescale thermostat/Parrinello-Rahman barostat. Motion equations were integrated by leapfrog algorithm with a time step of 1.0 fs. Three-dimensional periodic boundary conditions were always considered.

A hydrogen bond is recognized when the following two criteria are simultaneously met: (1) the distance between donor and acceptor atoms is within 0.35 nm, and (2) the angle of hydrogen-donor-acceptor is less than 30 degrees. Autocorrelation functions of the hydrogen-bond existence functions (either 0 or 1) were first defined according to following equation:

$$C(\tau) = \langle s_i(t) s_i(t+\tau) \rangle \quad (1)$$

with  $s_i(t) = \{0, 1\}$  for H-bond ( $i$ ) at time ( $t$ ).

Then the HB lifetime was estimated from the integral of  $C(\tau)$ :

$$\tau_{HB} = \int_0^{\infty} C(\tau) d\tau \quad (2)$$

Quantum chemical calculations were conducted at the b3lyp/6-31 g (d,p) level utilizing the density functional theory (DFT) method within the Gaussian 16 software. Concurrent frequency analysis was carried out to confirm the absence of imaginary frequency vibrations in all optimized structures. The electron energy for the optimized molecular configuration was determined using single point energy calculation (b3lyp/def2tzvp). The binding energy ( $E_b$ ) between molecules A and B was defined and calculated as follows:

$$E_b = E_{A+B} - E_A - E_B \quad (3)$$

where  $E_{A+B}$  represents the total energy of the molecular complex, while  $E_A$  and  $E_B$  denote the energies of the individual molecules A and B, respectively.

## 2.2. Physicochemical characterization of the $H_2O$ -TMP hybrid electrolyte

A series of  $H_2O$ -TMP hybrid electrolytes with different molar ratios of  $H_2O$  and TMP (1:0, 1:1, 1:2, 1:5, 1:10, respectively) and a constant  $NaClO_4$  concentration (0.6 mol L<sup>-1</sup>) were used as electrolytes. The structure of the hybrid electrolytes was characterized by Fourier transform infrared spectroscopy (FTIR) spectroscopy (Tensor 27, Bruker), Raman spectroscopy (HR evolution, Horiba Jobin Yvon, France), and <sup>1</sup>H and <sup>17</sup>O nuclear magnetic resonance (NMR) spectroscopy (Agilent 600 MHz). The viscosity was measured with a rotational rheometer (Kinexus pro, Malvern, England). In order to measure the ion conductivity, two stainless-steel-plate electrodes were inserted into the electrolytes as the block electrodes, and the corresponding ionic conductivity ( $\sigma$ ) was calculated using the Eq. (4):

$$\sigma = \frac{L}{A \times R} \quad (4)$$

where L and A are the distance between two stainless-steel electrodes (6.3 mm) and the area of the stainless-steel block electrode (1.27 cm<sup>2</sup>), respectively, while R is the electrolytic resistance obtained.

## 3. Results and discussion

### 3.1. Theoretical investigations

TMP is a type of aprotic organic solvent with higher Gutmann donors of 23 kcal mol<sup>-1</sup> than that of  $H_2O$ . Such water-miscible feature guarantee that it can serve as the proton acceptor to bond with the  $H_2O$  molecules and thus destroy the original HB network in traditional

aqueous electrolyte to restrict the  $H_2O$  activity [38]. Therefore, TMP was chosen as the proof-of-concept cosolvent in this work. To improve the ion conductivity of the aqueous-aprotic hybrid electrolyte, a fixed amount of  $NaClO_4$  was added considering its low price, earth abundance, and high solubility in both  $H_2O$  and TMP [30]. A series of  $H_2O$ -TMP hybrid electrolytes were prepared with different molar ratios of  $H_2O$  and TMP (1:0, 1:1, 1:2, 1:5, 1:10, respectively) and a constant  $NaClO_4$  concentration (0.6 mol L<sup>-1</sup>).

To explore the relationship between the electrolyte compositions, HB network, and the system properties, molecular dynamics (MD) simulations were first carried out. The snapshots of different hybrid electrolytes are shown in Fig. 1b and several critical parameters can be extracted and analyzed from the MD trajectories. Primarily, the total HB numbers in the  $H_2O$ -TMP hybrid electrolytes gradually decrease with the increasing TMP concentration, which is attributed to less and less  $H_2O$  content (Fig. S1). When the HB number per  $H_2O$  is considered, yet it exhibits an ascendant tendency (Fig. 1c). This variation originates from the destruction of the original intermolecular HB network between  $H_2O$  and  $H_2O$  and the formation of the new HB network between  $H_2O$  and TMP. Apparently, the higher the TMP concentration, the more HB are formed between TMP and  $H_2O$ , thus effectively confining the  $H_2O$  molecules. Meanwhile, the HB lifetime continues to prolong with the addition of TMP, which indicates the better stability of the newly formed  $H_2O$ -TMP HB in the hybrid electrolytes. This deduction can further be confirmed by the calculated binding energies and enthalpies of  $H_2O$ - $H_2O$  and  $H_2O$ -TMP HB as shown in Fig. 1d. Both the binding energy of -24.92 kJ mol<sup>-1</sup> and enthalpy of -31.24 kJ mol<sup>-1</sup> for  $H_2O$ -TMP are larger than those of -20.31 and -23.66 kJ mol<sup>-1</sup> for  $H_2O$ - $H_2O$ , respectively, illustrating that the  $H_2O$ -TMP HB is easier to form and more stable compared with that of  $H_2O$ - $H_2O$  HB [40–43]. The mean square displacement (MSD) was then utilized to assess the diffusion rate of  $H_2O$  in different electrolytes. As shown in Fig. 1e, the diffusion coefficient of  $H_2O$  reduces obviously when TMP is added gradually into the electrolytes, verifying the efficient limitation of the  $H_2O$  mobility. In a word, the original HB network tends to reshape via the newly formed  $H_2O$ -TMP HB, and more  $H_2O$  molecules are captured and confined around TMP molecules, thus greatly decreasing the water activity and inhibiting the transport of protons through the Grotthuss diffusion mechanism [37].

### 3.2. Physicochemical characterizations

To further understand the limited  $H_2O$  activity via the reconstruction of the HB network, the structure of the hybrid electrolyte was investigated by FTIR, Raman spectroscopy, and NMR. The full FTIR spectra is provided in Fig. S2 and several typical band areas are magnified in Fig. 2a. With increasing TMP content in the hybrid electrolyte, the stretching peak of P-O-(C) and (P)-O-C located at about 850 and 1040 cm<sup>-1</sup> show an obvious redshift, while the P=O stretching peak at 1260–1280 cm<sup>-1</sup> undergoes a blueshift, implying the intensified intermolecular HB interaction between TMP and  $H_2O$  [44,45]. The O-H bending vibration (1550–1850 cm<sup>-1</sup>) is gradually decreased, which is in line with the less  $H_2O$  content. Meanwhile, the minor redshift of this bending vibration also infers that the newly formed HB network influences the molecule structure of  $H_2O$  [43]. Worth mentioning that a distinct decrease in the intensity and blueshift of the O-H stretching vibration in 3200–3700 cm<sup>-1</sup> can also be observed. The higher wavenumber of light absorbed by O-H bond of  $H_2O$  molecules indicates the increased strength of O-H covalent bond in the newly formed HB network.

The reshaped HB network is also supported by the Raman spectroscopy (Fig. S3). As shown in Fig. 2b, two broad peaks located at about 736 and 752 cm<sup>-1</sup> corresponding to the stretching vibration of P-O-(C) and (P)-O-C groups of TMP, respectively, shift to lower wavenumber with the increased TMP content. At the same time, the P=O stretching mode located at about 1278 cm<sup>-1</sup> shift to higher wavenumbers [39,46].

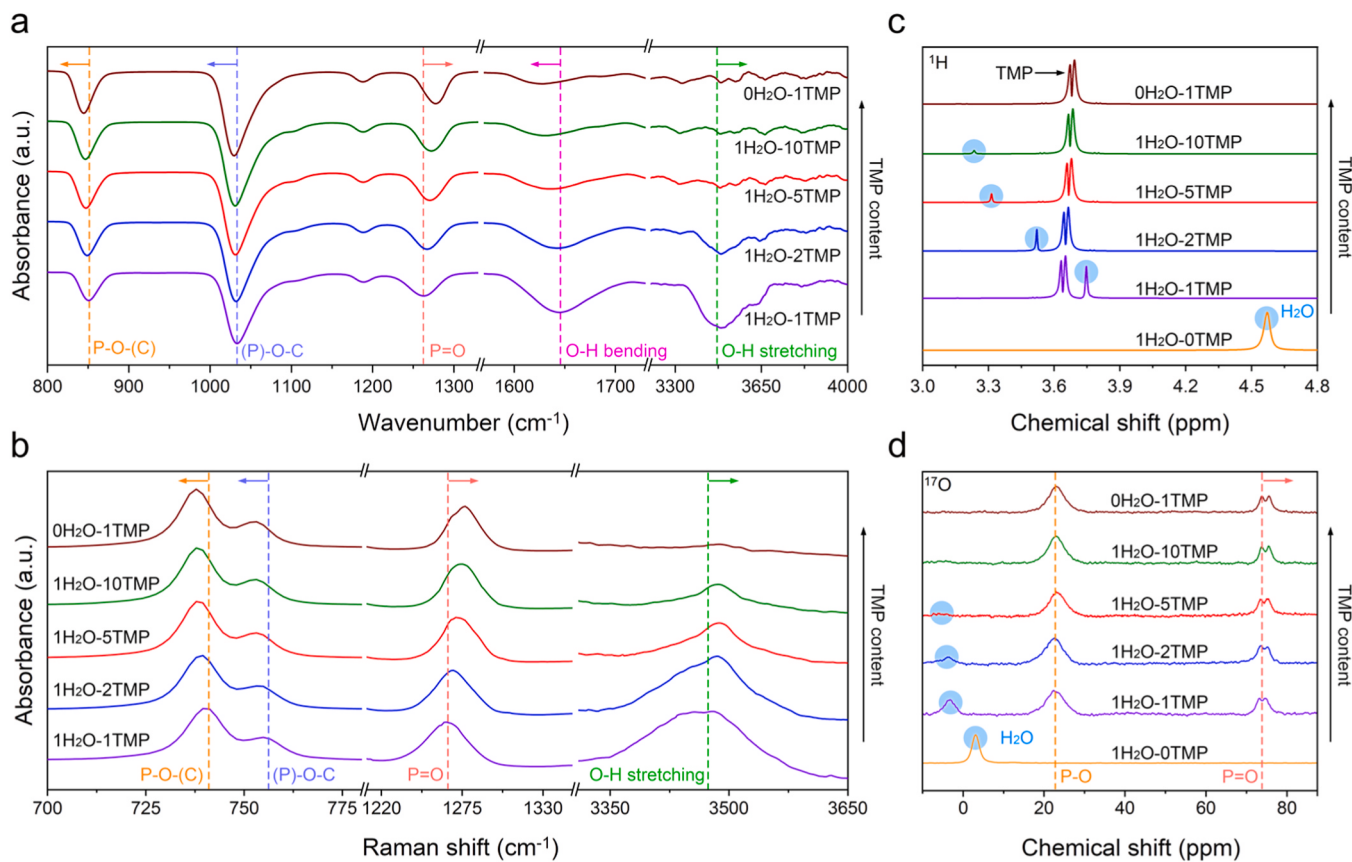


**Fig. 2.** (a) Fourier transform infrared spectroscopy, (b) Raman spectroscopy, (c)  $^1\text{H}$  nuclear magnetic resonance spectra, and (d)  $^{17}\text{O}$  nuclear magnetic resonance spectra of different electrolytes.

For the O-H stretching mode at the range from 3100 to 3700  $\text{cm}^{-1}$ , a significantly decreased signal intensity can be observed and the band area also presents a blueshift. These changes are in line with the variations observed in FTIR spectra. Based on the higher electron-donating ability of TMP than  $\text{H}_2\text{O}$ , the H of O-H in  $\text{H}_2\text{O}$  molecules prefer to interact with O of P=O bond in TMP molecules rather than adjacent  $\text{H}_2\text{O}$  molecules, forming the HB between TMP and  $\text{H}_2\text{O}$  (P=O-H-O). The role of TMP serving as an HB acceptor can additionally be validated through  $^1\text{H}$  NMR spectra (Fig. 2c). With the introduction of TMP, the chemical shift of H in  $\text{H}_2\text{O}$  molecules experiences a gradual downshift displacement, along with a minor upshift displacement of the H in TMP, reflecting a stronger electronic density in  $\text{H}_2\text{O}$ . This is attributed to the strong HB interaction between TMP and  $\text{H}_2\text{O}$ , which also affects the electron density around the P=O of TMP, as the downshift of P=O covalent bond in TMP can be observed in the  $^{17}\text{O}$  NMR spectra (Fig. 2d). The intensified HB between  $\text{H}_2\text{O}$  and TMP weakens the interaction between  $\text{H}_2\text{O}$  and  $\text{H}_2\text{O}$ , which strengthens the O-H covalent bond and makes it more difficult to be broken [47,48]. Therefore, the dissociation of the  $\text{H}_2\text{O}$  (Volmer step) can be greatly inhibited, leading to a suppressed HER activity in the hybrid electrolyte [49,50,54].

Walden plots can be drawn on the basis of the viscosity and ion conductivity data of different electrolytes (Fig. S4), which are shown in Fig. 3a. The  $\text{H}_2\text{O}$ -TMP hybrid electrolytes all fall below the bench line, originating from the intensified intermolecular interaction between  $\text{H}_2\text{O}$  and TMP, which further prevents the independent motion of protons in the hybrid electrolytes and thus inhibits HER effectively [51]. The electrochemical experiments were subsequently conducted to give direct evidence. Rh has been theoretically proven to be able to deliver excellent NRR performance, which can be further improved by the introduction of the second metal. Thus, RhCoNC with highly exposed RhCo active sites and excellent physicochemical properties derived from

MOF was synthesized as the model catalyst here and used for the following electrochemical measurements (Figs. S5-9). Linear sweep voltammograms (LSVs) were measured to compare the HER activity of the different electrolyte systems (Fig. 3b). The hydrogen evolution potential decreases with the increased TMP concentration, indicating that the addition of TMP indeed restrains the decomposition of  $\text{H}_2\text{O}$  and thus efficiently suppresses the HER process. Quantitative analysis was also carried out by gas chromatography and the hydrogen yield rates keep declining with increasing the TMP content (Fig. 3c). The Tafel slopes are derived from the LSV curves to further understand the reaction kinetics (Fig. 3d). The value of Tafel slope gradually increases with the increase of TMP concentration and the Tafel slope of the hybrid electrolytes are much larger than that without TMP, confirming  $\text{H}_2\text{O}$ -TMP HB network to be an efficient suppressor of the HER.

### 3.3. Catalytic nitrogen reduction

Subsequently, the electrochemical NRR experiments were carried out in a H-type cell separated by a Celgard membrane with hydrophilic pretreatment. An absorption cell filled with 0.1 M HCl was connected with the cathode chamber to avoid the volatilization of the formed  $\text{NH}_3$ . Before the electrochemical measurements, all feeding gases were purified sufficiently to remove any possible presence of  $\text{NH}_3$  or  $\text{NO}_x$  contaminants (Figs. S10-13). The NRR performance in different electrolyte systems were quantified by chronoamperometry at various potentials for 1 hour (Fig. S14). The produced  $\text{NH}_3$  and possible byproduct hydrazine were detected spectrophotometrically and only  $\text{NH}_3$  was detected after NRR electrolysis in this work (Figs. S15-17). The calculated  $\text{NH}_3$  yield rates and Faradaic efficiencies as a function of applied potential from -1.3 V to -1.7 V vs. Ag/AgCl are presented in Fig. 4a and b. As demonstrated above, the HER activity would be gradually suppressed

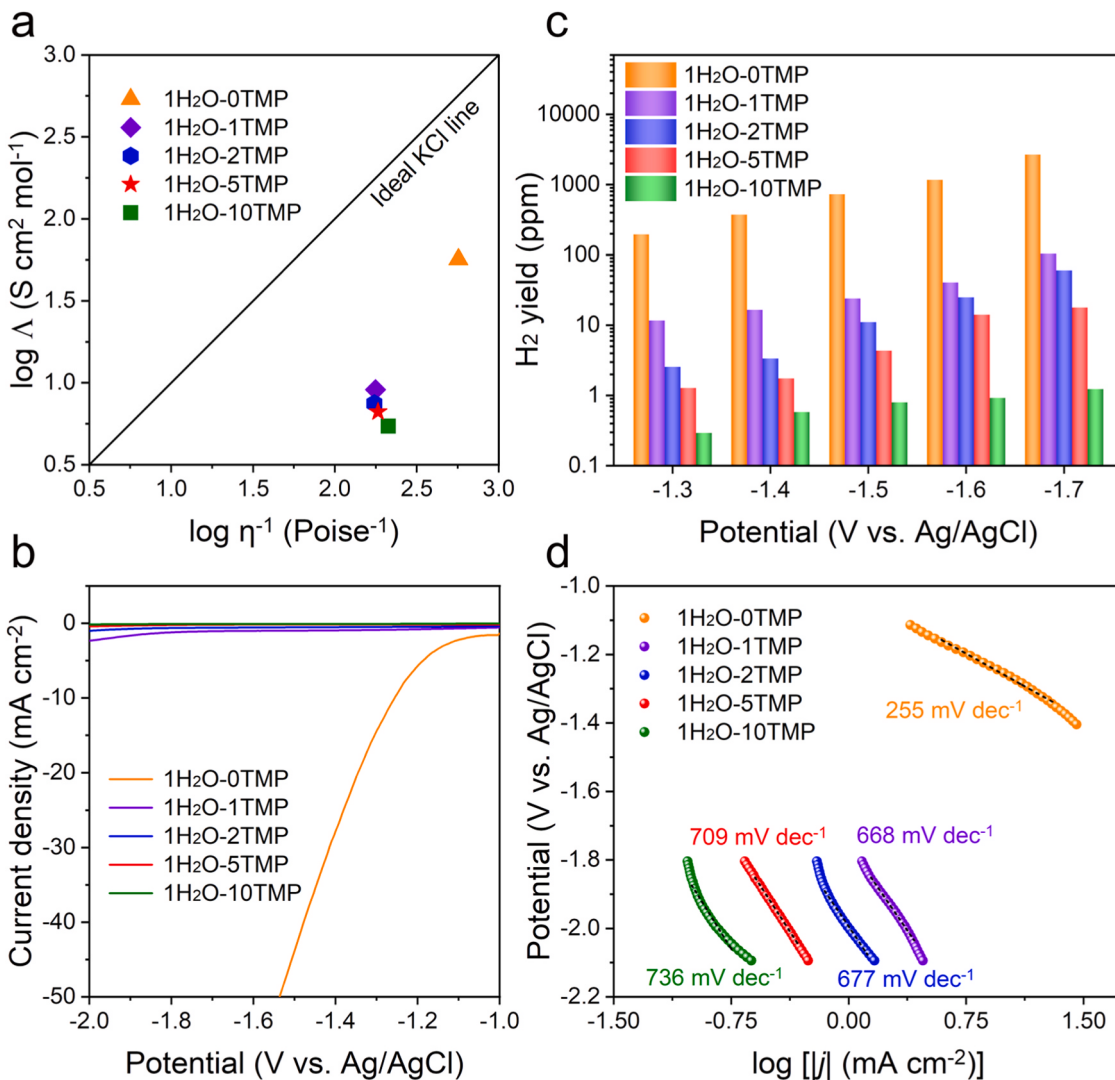


**Fig. 3.** (a) Walden plot showing relationships between inverse viscosity and molar conductivity for the H<sub>2</sub>O-TMP hybrid electrolytes with different molar ratios. (b) Linear sweep voltammograms, (c) HER yield rates, and (d) Tafel plots in the H<sub>2</sub>O-TMP hybrid electrolytes with different molar ratios.

with the presence of TMP due to the reshaping of HB network. With the increase of TMP concentration, not only the amount of water available in the electrolyte is reduced, but also the generation of intensified HB between TMP and H<sub>2</sub>O enhance the strength of O-H covalent bond in water, making it more difficult to be broken, so that the dissociation of water is further inhibited. Correspondingly, the NRR performance exhibits an opposite trend and achieves gradual improvement with increasing TMP content. Interestingly, the NH<sub>3</sub> yield rate meet the maximum value in the 1H<sub>2</sub>O-5TMP electrolyte, with a superior NH<sub>3</sub> yield rate of  $82.1 \pm 2.7 \mu\text{g h}^{-1} \text{mg}^{-1}$  obtained at  $-1.5 \text{ V}$  vs. Ag/AgCl combined with the optimum Faradaic efficiency of  $73.3 \pm 2.7\%$ . The NRR performance was further examined via ion chromatography method. Upon quantification, the NH<sub>3</sub> yield rate is  $79.5 \mu\text{g h}^{-1} \text{mg}^{-1}$  and the Faradaic efficiency is 71.8%, which are close to those obtained from the indophenol blue method, verifying the reliability of our results. As the amount of TMP continues to increase and the molar ratio of H<sub>2</sub>O-TMP is up to 1:10, the H<sub>2</sub>O activity is limited to an extremely low level, which in turn hinders the hydrogenation process of NRR as proton-coupled electron transfer reaction. As a result, although the HER is further suppressed, a diminution of the NRR performance is also observed in the 1H<sub>2</sub>O-10TMP electrolyte. That is, the accessibility of free water should be controlled to be neither too high to inhibit the HER nor too low since the lack of proton supply will still limit the NRR activity.

In situ Raman characterizations were then applied to monitor the whole NRR process in the 1H<sub>2</sub>O-0TMP and 1H<sub>2</sub>O-5TMP electrolytes. In the 1H<sub>2</sub>O-5TMP electrolyte, two Raman peaks at approximately 1150 and 1520 cm<sup>-1</sup>, assigned to -NH<sub>2</sub> and -NH, respectively, gradually appear and increase in intensity as the reaction progressed, while the two peaks at about 1248 and 1432 cm<sup>-1</sup> attributable to the feature peak of TMP do not have any obvious change (Fig. 4c) [52]. On the contrary, no intermediate-related peak was detected when the same experiment was performed in the 1H<sub>2</sub>O-0TMP electrolyte (Fig. 4d), which can be explained by the unfavored NRR process. The in situ observations provide a further verification on the efficient promotion effect of TMP on the NRR performance. To further ensure the authenticity of the production of NH<sub>3</sub>, <sup>15</sup>N isotope labelling experiments were conducted (Fig. S18) [53]. As illustrated in Fig. 4e, the <sup>1</sup>H NMR spectra only exist a doublet signal representing <sup>15</sup>NH<sub>4</sub><sup>+</sup> when <sup>15</sup>N<sub>2</sub> is used as feeding gas, demonstrating that the feeding gas is the only nitrogen source for the electrochemical NH<sub>3</sub> synthesis. Excellent stability of RhCoNC electrocatalyst was observed in this electrochemical system, with no obvious loss of Faradaic efficiency or NH<sub>3</sub> yield rate for five successive cycles (Fig. S19). After long-term electrolysis, 1H<sub>2</sub>O-5TMP electrolyte was carefully characterized by FTIR and Raman spectra, and the results indicate that the properties of the aqueous-aprotic hybrid electrolyte system remain unchanged during the electrochemical measurements

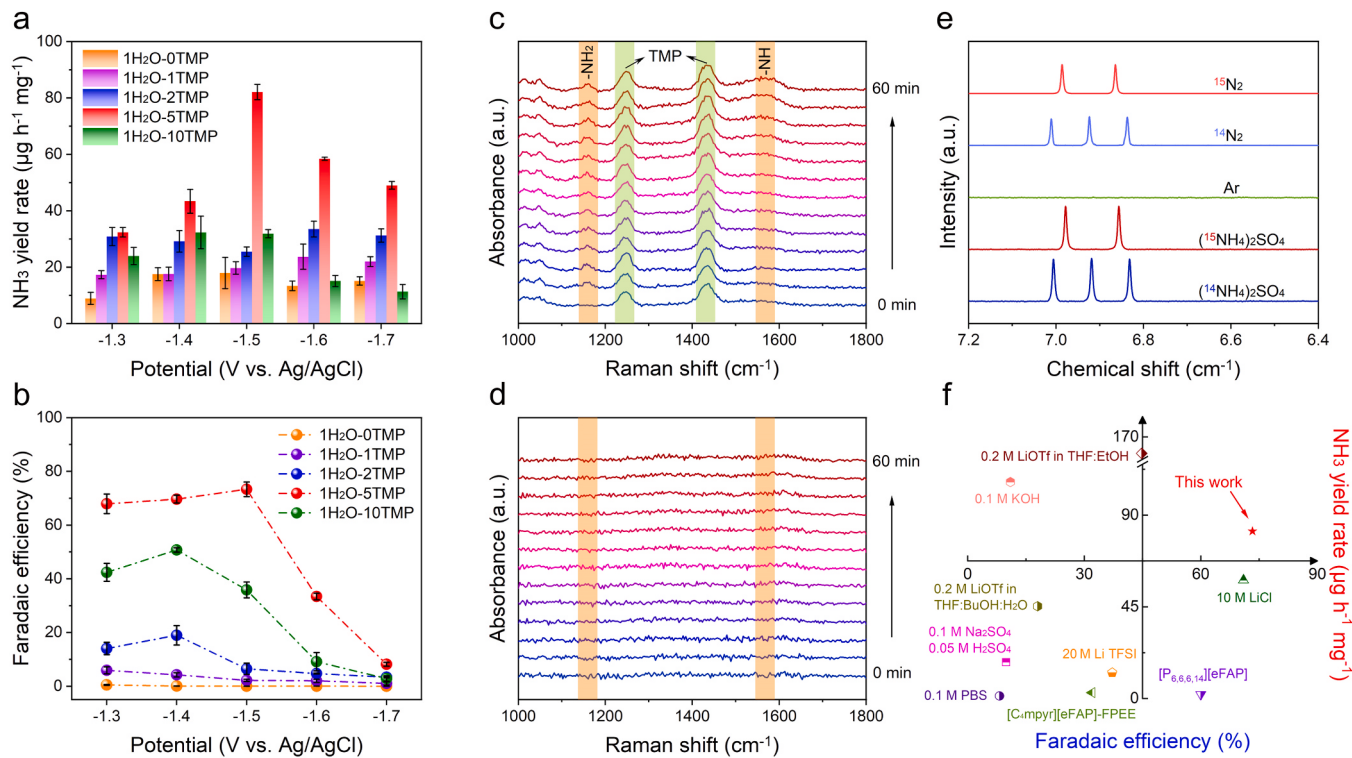


**Fig. 4.** (a) NH<sub>3</sub> yield rates and (b) corresponding Faradaic efficiencies in the H<sub>2</sub>O-TMP hybrid electrolytes with different molar ratios. In situ Raman spectra in the (c) 1H<sub>2</sub>O-5TMP and (d) 1H<sub>2</sub>O-0TMP electrolytes at the potential of -1.5 V vs. Ag/AgCl as a function of time. (e) <sup>1</sup>H NMR spectra of the NRR products using different feed gases at -1.5 V vs. Ag/AgCl in the 1H<sub>2</sub>O-5TMP electrolyte. (f) Comparison of our results with state-of-the-art reports focusing on electrolyte design in terms of yield rate and Faradaic efficiency; detailed data are provided in Table S1.

(Fig. S20). Comparing the excellent NRR performance obtained in the hybrid electrolyte with several typical reports, it ranks among the best of the state-of-the-art work focusing on electrolyte design (Fig. 4f, Table S1).

#### 4. Conclusion

In summary, the introduction of TMP as a cosolvent gave rise to a novel aqueous-aprotic hybrid electrolyte system for highly selective ammonia synthesis under ambient conditions. The critical role of TMP was firstly highlighted by the MD simulations, which demonstrate that, the higher the TMP concentration, the more HB are formed between TMP and H<sub>2</sub>O, and the longer the HB lifetime. The reshaped HB network enables effective confinement of the H<sub>2</sub>O molecules, thus greatly decreasing the water activity. Physicochemical characterization of the hybrid electrolyte confirmed the formation of reshaped HB network, in which the intensified HB between H<sub>2</sub>O and TMP weakens the interaction between H<sub>2</sub>O and H<sub>2</sub>O, strengthening the O-H bond in H<sub>2</sub>O and making it more difficult to be broken. Therefore, the dissociation of the H<sub>2</sub>O (Volmer step) can be greatly inhibited, leading to a suppressed HER activity in the hybrid electrolyte. As expected, a superior NH<sub>3</sub> yield rate of  $82.1 \pm 2.7 \mu\text{g h}^{-1} \text{mg}^{-1}$  with the optimum Faradaic efficiency of  $73.3 \pm 2.7\%$  were obtained at -1.5 V vs. Ag/AgCl in the H<sub>2</sub>O-TMP hybrid electrolyte, ranking among the best of the state-of-the-art work focusing on electrolyte design. This study highlights the promise of a successful electrolyte design for the development of practical ammonia synthesis.

#### CRediT authorship contribution statement

**Qiyang Cheng:** Software, Data curation. **Jiajie Ni:** Writing – original draft, Investigation, Data curation. **Haoqing Ji:** Software, Data curation. **Sisi Liu:** Writing – original draft, Investigation. **Mengfan Wang:** Writing – original draft, Data curation. **Jianmei Lu:** Writing – review &

editing, Visualization, Conceptualization. **Chenglin Yan:** Writing – review & editing, Visualization, Funding acquisition. **Tao Qian:** Supervision. **Yanzheng He:** Investigation.

#### Declaration of Competing Interest

The authors declare that they have no known competing financial interests or personal relationships that could have appeared to influence the work reported in this paper.

#### Data availability

Data will be made available on request.

#### Acknowledgements

This work was supported by the National Natural Science Foundation of China [No. U21A20332, 5210322, 52202275, 52203314, and 12204253] and the Distinguished Young Scholars Fund of Jiangsu Province [No. BK20220061].

#### Appendix A. Supporting information

Supplementary data associated with this article can be found in the online version at [doi:10.1016/j.apcatb.2024.123944](https://doi.org/10.1016/j.apcatb.2024.123944).

#### References

- [1.] N. Gruber, J.N. Galloway, An earth-system perspective of the global nitrogen cycle, *Nature* 451 (2008) 293–296, <https://doi.org/10.1038/nature06592>.
- [2.] S. Liu, Y. Jiang, M. Wang, Y. Huan, Y. He, Q. Cheng, Y. Cheng, J. Liu, X. Zhou, T. Qian, C. Yan, Awakening (220) as one more active facet of PtMo alloy via single-atom doping to boost ammonia electrooxidation in direct ammonia fuel cell, *Adv. Funct. Mater.* 33 (2023) 2306204, <https://doi.org/10.1002/adfm.202306204>.

[3.] D.R. MacFarlane, P.V. Cherepanov, J. Choi, B.H.R. Suryanto, R.Y. Hodgetts, J. M. Bakker, F.M. Ferrero Vallana, A.N. Simonov, A roadmap to the ammonia economy, Joule 4 (2020) 1186–1205, <https://doi.org/10.1016/j.joule.2020.04.004>.

[4.] H. Yu, Y. Xue, L. Hui, C. Zhang, Y. Fang, Y. Liu, X. Chen, D. Zhang, B. Huang, Y. Li, Graphdiyne-based metal atomic catalysts for synthesizing ammonia, Natl. Sci. Rev. 8 (2021) nwaa213, <https://doi.org/10.1093/nsr/nwaa213>.

[5.] M. Wang, S. Liu, T. Qian, J. Liu, J. Zhou, H. Ji, J. Xiong, J. Zhong, C. Yan, Over 56.55% Faradaic efficiency of ambient ammonia synthesis enabled by positively shifting the reaction potential, Nat. Commun. 10 (2019) 341, <https://doi.org/10.1038/s41467-018-08120-x>.

[6.] C. Wang, Q. Cheng, M. Wang, S. Liu, Y. He, C. Deng, Y. Sun, T. Qian, N. Xu, F. Rosei, C. Yan, Asymmetric electrode design with built-in nitrogen transfer channel achieving maximized three-phase reaction region for electrochemical ammonia synthesis, Electron 1 (2023) e2, <https://doi.org/10.1002/elt2.2>.

[7.] C. Smith, L. Torrente-Murciano, Exceeding single-pass equilibrium with integrated absorption separation for ammonia synthesis using renewable energy—redefining the Haber-Bosch loop, Adv. Energy Mater. 11 (2021) 2003845, <https://doi.org/10.1002/aenm.202003845>.

[8.] S. Liu, M. Wang, Q. Cheng, Y. He, J. Ni, J. Liu, C. Yan, T. Qian, Turning waste into wealth: sustainable production of high-value-added chemicals from catalytic coupling of carbon dioxide and nitrogenous small molecules, ACS Nano 16 (2022) 17911–17930, <https://doi.org/10.1021/acsnano.2c09168>.

[9.] R. Li, Y. Bian, C. Yang, L. Guo, T. Ma, C. Wang, F. Fu, D. Wang, Electronic structure regulation and built-in electric field synergistically strengthen photocatalytic nitrogen fixation performance on Ti-BiO<sub>3</sub>/TiO<sub>2</sub> heterostructure, Rare Met. (2023), <https://doi.org/10.1007/s12598-023-02471-1>.

[10.] Y. He, S. Liu, M. Wang, H. Ji, L. Zhang, Q. Cheng, T. Qian, C. Yan, Advancing the electrochemistry of gas-involved reactions through theoretical calculations and simulations from microscopic to macroscopic, Adv. Funct. Mater. 32 (2022) 2208474, <https://doi.org/10.1002/adfm.202208474>.

[11.] F. Jiao, B. Xu, Electrochemical ammonia synthesis and ammonia fuel cells, Adv. Mater. 31 (2019) 1805173, <https://doi.org/10.1002/adma.201805173>.

[12.] S. Liu, T. Qian, M. Wang, H. Ji, X. Shen, C. Wang, C. Yan, Proton-filtering covalent organic frameworks with superior nitrogen penetration flux promote ambient ammonia synthesis, Nat. Catal. 4 (2021) 322–331, <https://doi.org/10.1038/s41929-021-00599-w>.

[13.] T.-N. Ye, S.-W. Park, Y. Lu, J. Li, M. Sasase, M. Kitano, T. Tada, H. Hosono, Vacancy-enabled N<sub>2</sub> activation for ammonia synthesis on an Ni-loaded catalyst, Nature 583 (2020) 391–395, <https://doi.org/10.1038/s41586-020-2464-9>.

[14.] S. Liu, M. Wang, Y. He, Q. Cheng, H. Ji, T. Qian, C. Yan, Molecularly imprinting technology enables proactive capture of nitrogen for boosted ammonia synthesis under ambient conditions, Adv. Mater. 35 (2023) 2303703, <https://doi.org/10.1002/adma.202303703>.

[15.] C. Guo, J. Ran, A. Vasileff, S.-Z. Qiao, Rational design of electrocatalysts and photo (electro)catalysts for nitrogen reduction to ammonia (NH<sub>3</sub>) under ambient conditions, Energy Environ. Sci. 11 (2018) 45–56, <https://doi.org/10.1039/C7EE02220D>.

[16.] Y. Jiang, M. Wang, L. Zhang, S. Liu, Y. Cao, S. Qian, Y. Cheng, X. Xu, C. Yan, T. Qian, Distorted spinel ferrite heterostructure triggered by alkaline earth metal substitution facilitates nitrogen localization and electrocatalytic reduction to ammonia, Chem. Eng. J. 450 (2022) 138226, <https://doi.org/10.1016/j.cej.2022.138226>.

[17.] Z. Huang, M. Rafiq, A.R. Woldu, Q.-X. Tong, D. Astruc, L. Hu, Recent progress in electrocatalytic nitrogen reduction to ammonia (NRR), Coord. Chem. Rev. 478 (2023) 214981, <https://doi.org/10.1016/j.ccr.2022.214981>.

[18.] Q. Cheng, M. Wang, J. Ni, Y. He, H. Ji, S. Liu, C. Yan, High-entropy alloys for accessing hydrogen economy via sustainable production of fuels and direct application in fuel cells, Rare Met. 42 (2023) 3553–3569, <https://doi.org/10.1007/s12598-023-02343-8>.

[19.] X. Li, J. Wang, One-dimensional and two-dimensional synergized nanostructures for high-performing energy storage and conversion, InfoMat 2 (2020) 3–32, <https://doi.org/10.1002/inf2.12040>.

[20.] S. Liu, M. Wang, H. Ji, X. Shen, C. Yan, T. Qian, Altering the rate-determining step over cobalt single clusters leading to highly efficient ammonia synthesis, Natl. Sci. Rev. 8 (2021) nwaa136, <https://doi.org/10.1093/nsr/nwaa136>.

[21.] H. He, H.-M. Wen, H.-K. Li, P. Li, J. Wang, Y. Yang, C.-P. Li, Z. Zhang, M. Du, Hydrophobicity tailoring of ferris covalent organic framework/MXene nanosheets for high-efficiency nitrogen electroreduction to ammonia, Adv. Sci. 10 (2023) 2206933, <https://doi.org/10.1002/advs.202206933>.

[22.] S. Liu, M. Wang, T. Qian, H. Ji, J. Liu, C. Yan, Facilitating nitrogen accessibility to boron-rich covalent organic frameworks via electrochemical excitation for efficient nitrogen fixation, Nat. Commun. 10 (2019) 3898, <https://doi.org/10.1038/s41467-019-11846-x>.

[23.] Y. He, M. Wang, S. Liu, L. Zhang, Q. Cheng, C. Yan, T. Qian, A superaerophilic gas diffusion electrode enabling facilitated nitrogen feeding through hierarchical micro/nano channels for efficient ambient synthesis of ammonia, Chem. Eng. J. 454 (2023) 140106, <https://doi.org/10.1016/j.cej.2022.140106>.

[24.] X. Shen, S. Liu, X. Xia, M. Wang, H. Ji, Z. Wang, J. Liu, X. Zhang, C. Yan, T. Qian, Interfacial microextraction boosting nitrogen feed for efficient ambient ammonia synthesis in aqueous electrolyte, Adv. Funct. Mater. 32 (2022) 2109422, <https://doi.org/10.1002/adfm.202109422>.

[25.] P. Shen, X. Li, Y. Luo, Y. Guo, X. Zhao, K. Chu, High-efficiency N<sub>2</sub> electroreduction enabled by Se-vacancy-rich WSe<sub>2-x</sub> in water-in-salt electrolytes, ACS Nano 16 (2022) 7915–7925, <https://doi.org/10.1021/acsnano.2c00596>.

[26.] J. Ni, Q. Cheng, S. Liu, M. Wang, Y. He, T. Qian, C. Yan, J. Lu, Deciphering electrolyte selection for electrochemical reduction of carbon dioxide and nitrogen to high-value-added chemicals, Adv. Funct. Mater. 33 (2023) 2212483, <https://doi.org/10.1002/adfm.202212483>.

[27.] S. Liu, M. Wang, H. Ji, L. Zhang, J. Ni, N. Li, T. Qian, C. Yan, J. Lu, Solvent-in-gas system for promoted photocatalytic ammonia synthesis on porous framework materials, Adv. Mater. 35 (2023) 2211730, <https://doi.org/10.1002/adma.202211730>.

[28.] C. He, Z. Wu, L. Zhao, M. Ming, Y. Zhang, Y. Yi, J. Hu, Identification of FeN<sub>4</sub> as an efficient active site for electrochemical N<sub>2</sub> reduction, ACS Catal. 9 (2019) 7311–7317, <https://doi.org/10.1021/acscatal.9b00959>.

[29.] U.K. Ghorai, S. Paul, B. Ghorai, A. Adalder, S. Kapse, R. Thapa, A. Nagendra, A. Gain, Scalable production of cobalt phthalocyanine nanotubes: efficient and robust hollow electrocatalyst for ammonia synthesis at room temperature, ACS Nano 15 (2021) 5230–5239, <https://doi.org/10.1021/acsnano.0c10596>.

[30.] Y. He, S. Liu, M. Wang, Q. Cheng, T. Qian, C. Yan, Deciphering engineering principle of three-phase interface for advanced gas-involved electrochemical reactions, J. Energy Chem. 80 (2023) 302–323, <https://doi.org/10.1016/j.jechem.2023.02.002>.

[31.] D. Chen, R. Yu, R. Lu, Z. Pu, P. Wang, J. Zhu, P. Ji, D. Wu, J. Wu, Y. Zhao, Z. Kou, J. Yu, S. Mu, Tunable Ru-Ru<sub>2</sub>P heterostructures with charge redistribution for efficient pH-universal hydrogen evolution, InfoMat 4 (2022) e12287, <https://doi.org/10.1002/inf2.12287>.

[32.] S. Murmu, S. Paul, S. Kapse, R. Thapa, S. Chattopadhyay, A.N. S. N. D. Jha, U. K. Bhattacharyya, Ghorai, Unveiling the genesis of the high catalytic activity in nickel phthalocyanine for electrochemical ammonia synthesis, J. Mater. Chem. A 9 (2021) 14477–14484, <https://doi.org/10.1039/DITA00766A>.

[33.] Q. Cheng, M. Wang, S. Liu, L. Zhang, H. Ji, Y. He, N. Li, T. Qian, C. Yan, J. Lu, Eliminating concentration polarization with cationic covalent organic polymer to promote effective overpotential of nitrogen fixation, Angew. Chem. Int. Ed. 62 (2023) e202308262, <https://doi.org/10.1002/anie.202308262>.

[34.] Y. Ren, C. Yu, X. Han, X. Tan, Q. Wei, W. Li, Y. Han, L. Yang, J. Qiu, Methanol-mediated electrosynthesis of ammonia, ACS Energy Lett. 6 (2021) 3844–3850, <https://doi.org/10.1021/acsenrglett.1c01893>.

[35.] Y. Wang, T. Wang, D. Dong, J. Xie, Y. Guan, Y. Huang, J. Fan, Y.-C. Lu, Enabling high-energy-density aqueous batteries with hydrogen bond-anchored electrolytes, Matter 5 (2022) 162–179, <https://doi.org/10.1016/j.matt.2021.10.021>.

[36.] Q. Nian, X. Zhang, Y. Feng, S. Liu, T. Sun, S. Zheng, X. Ren, Z. Tao, D. Zhang, J. Chen, Designing electrolyte structure to suppress hydrogen evolution reaction in aqueous batteries, ACS Energy Lett. 6 (2021) 2174–2180, <https://doi.org/10.1021/acsenrglett.1c00833>.

[37.] K. Lu, C. Chen, Y. Wu, C. Liu, J. Song, H. Jing, P. Zhao, B. Liu, M. Xia, Q. Hao, W. Lei, Versatile 1, 3-dimethyl-2-imidazolidinone electrolyte additive: Enables extremely long life zinc metal batteries with different substrates, Chem. Eng. J. 457 (2023) 141287, <https://doi.org/10.1016/j.cej.2023.141287>.

[38.] D. Marx, M.E. Tuckerman, J. Hutter, M. Parrinello, The nature of the hydrated excess proton in water, Nature 397 (1999) 601–604, <https://doi.org/10.1038/17579>.

[39.] B. Qiu, L. Xie, G. Zhang, K. Cheng, Z. Lin, W. Liu, C. He, P. Zhang, H. Mi, Toward reversible wide-temperature Zn storage by regulating the electrolyte solvation structure via trimethyl phosphate, Chem. Eng. J. 449 (2022) 137843, <https://doi.org/10.1016/j.cej.2022.137843>.

[40.] S. Wu, B. Su, M. Sun, S. Gu, Z. Lu, K. Zhang, D.Y.W. Yu, B. Huang, P. Wang, C.-S. Lee, W. Zhang, Dilute aqueous-aprotic hybrid electrolyte enabling a wide electrochemical window through solvation structure engineering, Adv. Mater. 33 (2021) 2102390, <https://doi.org/10.1002/adma.202102390>.

[41.] T.C. Li, Y. Lim, X.L. Li, S. Luo, C. Lin, D. Fang, S. Xia, Y. Wang, H.Y. Yang, A universal additive strategy to reshape electrolyte solvation structure toward reversible Zn storage, Adv. Energy Mater. 12 (2022) 2103231, <https://doi.org/10.1002/aenm.202103231>.

[42.] Q. Yuan, T. Zhou, L. Li, J. Zhang, X. Liu, X. Ke, A. Zhang, Hydrogen bond breaking of TPU upon heating: understanding from the viewpoints of molecular movements and enthalpy, RSC Adv. 5 (2015) 31153–31165, <https://doi.org/10.1039/C5RA03984C>.

[43.] L. Wen, J. Zhang, T. Zhou, A. Zhang, Hydrogen bonding in micro-phase separation of poly(polyamide 12-block-polytetrahydrofuran) alternating block copolymer: Enthalpies and molecular movements, Vib. Spectrosc. 86 (2016) 160–172, <https://doi.org/10.1016/j.vibspec.2016.07.001>.

[44.] C. Tang, M. Li, Y. Wang, Y. Zhang, Y. Yao, G. Wang, J. Liu, L. Li, Wide temperature range- and damage-tolerant microsupercapacitors from salt-tolerant, anti-freezing and self-healing organohydrogel via dynamic bonds modulation, J. Energy Chem. 78 (2023) 283–293, <https://doi.org/10.1016/j.jechem.2022.11.051>.

[45.] Q. Nian, J. Wang, S. Liu, T. Sun, S. Zheng, Y. Zhang, Z. Tao, J. Chen, Aqueous batteries operated at -50 °C, Angew. Chem. Int. Ed. 58 (2019) 16994–16999, <https://doi.org/10.1002/anie.201908913>.

[46.] Q. Li, C. Yang, J. Zhang, X. Ji, J. Xu, X. He, L. Chen, S. Hou, J. Uddin, D. Addison, D. Sun, C. Wang, F. Wang, Controlling intermolecular interaction and interphase chemistry enabled sustainable water-tolerance LiMn<sub>2</sub>O<sub>4</sub>||Li<sub>4</sub>Ti<sub>5</sub>O<sub>12</sub> batteries, Angew. Chem. Int. Ed. 61 (2022) e202214126, <https://doi.org/10.1002/anie.202214126>.

[47.] H. Nakagawa, M. Ochida, Y. Domi, T. Doi, S. Tsubouchi, T. Yamanaka, T. Abe, Z. Ogumi, Electrochemical Raman study of edge plane graphite negative-electrodes in electrolytes containing trialkyl phosphoric ester, J. Power Sources 212 (2012) 148–153, <https://doi.org/10.1016/j.jpowsour.2012.04.013>.

[48.] Q. Zhang, Y. Ma, Y. Lu, L. Li, F. Wan, K. Zhang, J. Chen, Modulating electrolyte structure for ultralow temperature aqueous zinc batteries, *Nat. Commun.* 11 (2020) 4463, <https://doi.org/10.1038/s41467-020-18284-0>.

[49.] N. Chang, T. Li, R. Li, S. Wang, Y. Yin, H. Zhang, X. Li, An aqueous hybrid electrolyte for low-temperature zinc-based energy storage devices, *Energy Environ. Sci.* 13 (2020) 3527–3535, <https://doi.org/10.1039/D0EE01538E>.

[50.] D. Strmcnik, P.P. Lopes, B. Genorio, V.R. Stamenkovic, N.M. Markovic, Design principles for hydrogen evolution reaction catalyst materials, *Nano Energy* 29 (2016) 29–36, <https://doi.org/10.1016/j.nanoen.2016.04.017>.

[51.] Y. Luo, L. Tang, U. Khan, Q. Yu, H.-M. Cheng, X. Zou, B. Liu, Morphology and surface chemistry engineering toward pH-universal catalysts for hydrogen evolution at high current density, *Nat. Commun.* 10 (2019) 269, <https://doi.org/10.1038/s41467-018-07792-9>.

[52.] P. Zou, R. Lin, T.P. Pollard, L. Yao, E. Hu, R. Zhang, Y. He, C. Wang, W.C. West, L. Ma, O. Borodin, K. Xu, X.-Q. Yang, H.L. Xin, Localized hydrophobicity in aqueous zinc electrolytes improves zinc metal reversibility, *Nano Lett.* 22 (2022) 7535–7544, <https://doi.org/10.1021/acs.nanolett.2c02514>.

[53.] S. Tsubouchi, S. Suzuki, K. Nishimura, T. Okumura, T. Abe, Effect of lewis acids on graphite-electrode properties in EC-based electrolyte solutions with organophosphorus compounds, *J. Electrochem. Soc.* 165 (2018) A680, <https://doi.org/10.1149/2.0621803jes>.

[54.] L. Zhang, H. Zhou, X. Yang, S. Zhang, H. Zhang, X. Yang, X. Su, J. Zhang, Z. Lin, Boosting electroreduction kinetics of nitrogen to ammonia via atomically dispersed Sn protuberance, *Angew. Chem. Int. Ed.* 62 (2023) e202217473, <https://doi.org/10.1002/anie.202217473>.